Drop impact onto pine needle fibers with non-circular cross section

Cite as: Phys. Fluids **32**, 092113 (2020); https://doi.org/10.1063/5.0019310
Submitted: 23 June 2020 . Accepted: 07 September 2020 . Published Online: 29 September 2020

Amy P. Lebanoff, and Andrew K. Dickerson

Physics of Fluids ARTICLE scitation.org/journal/phf

Drop impact onto pine needle fibers with non-circular cross section

Cite as: Phys. Fluids 32, 092113 (2020); doi: 10.1063/5.0019310
Submitted: 23 June 2020 • Accepted: 7 September 2020 •
Published Online: 29 September 2020

Amy P. Lebanoff and Andrew K. Dickerson[a)]

AFFILIATIONS

Department of Mechanical and Aerospace Engineering, University of Central Florida, Orlando, Florida 32816, USA

[a)]Author to whom correspondence should be addressed: dickerson@ucf.edu

ABSTRACT

Pine needles have evolved alongside rainfall for millennia. Needles are robust to raindrop impacts and the portions of mass impacting raindrops leave behind. Pine needles also provide a unique fiber profile by which to study liquid drop collisions on slender structures. In this experimental study, we use high-speed videography to film the impact of water drops onto green, rigidly supported *Pinus palustris* needles, which are of non-circular cross section. Impacts result in drop division into thin, ephemeral lobes, which collapse within milliseconds, splitting the parent drop. We measure orientation-dependent lobe shapes and separation angles, impact force, drop spreading on fibers, and mass retention. Lobes formed by impact with the rounded side of needles are parabolic in shape, while those with the wedged side are irregular. For a fixed drop size, impact forces on rounded surfaces are consistently less than those experienced by wedged surfaces, and the disparity in the impact force between the two orientations grows with the Weber number. The smaller of the two drop sizes on test is more effective at generating impact forces per drop weight than the larger drops. Post-impact, fibers in both orientations retain residual mass from the impacting drop. The wedged surface is more effective at splitting drops and shedding drop remnants.

I. INTRODUCTION

The impact of water drops with slender structures is spectacularly commonplace. Raindrops strike blades of grass, insect appendages,[1–4] cacti needles,[5] spider webs, and pine litter. In technological applications, the impact of drops with slender fibers occurs in spray coating and air filtration.[6] Generally, drop properties and the physical conditions of a substrate, such as surface roughness, texture, and chemistry, greatly influence post-impact dynamics for both broad and slender surfaces. For example, increased hydrophobicity imbues larger impact forces, rebound, and slightly limited spreading.[7–9] The drop viscosity demands a greater reduction in spreading by effectively dissipating kinetic energy.[9] On flat surfaces, the thickness of the spreading fluid lamella necessarily scales as the capillary length. At sufficient impact velocities, the advancing liquid sheet, post-impact, will become unstable and fragment into smaller drops.[7]

A number of experimental[10–19] and computational[20–25] studies of drop impact with fixed,[10–17,20,24,25] cantilevered,[18,19] and meshed[13,14] fibers have arisen in recent years. These previous studies can be classified into two groups, those which consider fiber diameters significantly smaller than drops[10,11,13–19,25] and those with diameters larger than drops.[12,20] The primary focus of some of these studies[11,17–20,24] has been to define the threshold for drop capture, which may occur at sufficiently low speeds and is improved by hydrophilicity, oblique impact angles, viscous dissipation, high surface tension, and tuned fiber flexibility. The capture speed threshold for cantilevered fibers increases when drops begin to recoil prior to the fiber rebound.[18,19] For impacts in which drops are not captured, drops may release as a single drop or fragment, often leaving residual mass on the fiber. The captured mass for fixed fibers is more dependent on the fiber size rather than the drop speed.[17] The drop speed, on the other hand, plays a major role in the impact regime; drops are either split apart, fall past the fiber as a unified mass, or are captured. Other studies have focused on mass retention,[15,17] detachment,[25] and dynamical characterization of impact regimes.[11,26] All of the aforementioned studies consider only fibers with circular cross section. The impact of drops on naturally relevant fibers remains uncharacterized. Our study is the first to consider drop impact on non-circular fibers, to our knowledge.

In this study, we impact fixed, non-circular fibers in two orientations with falling water drops to elucidate the impact force,

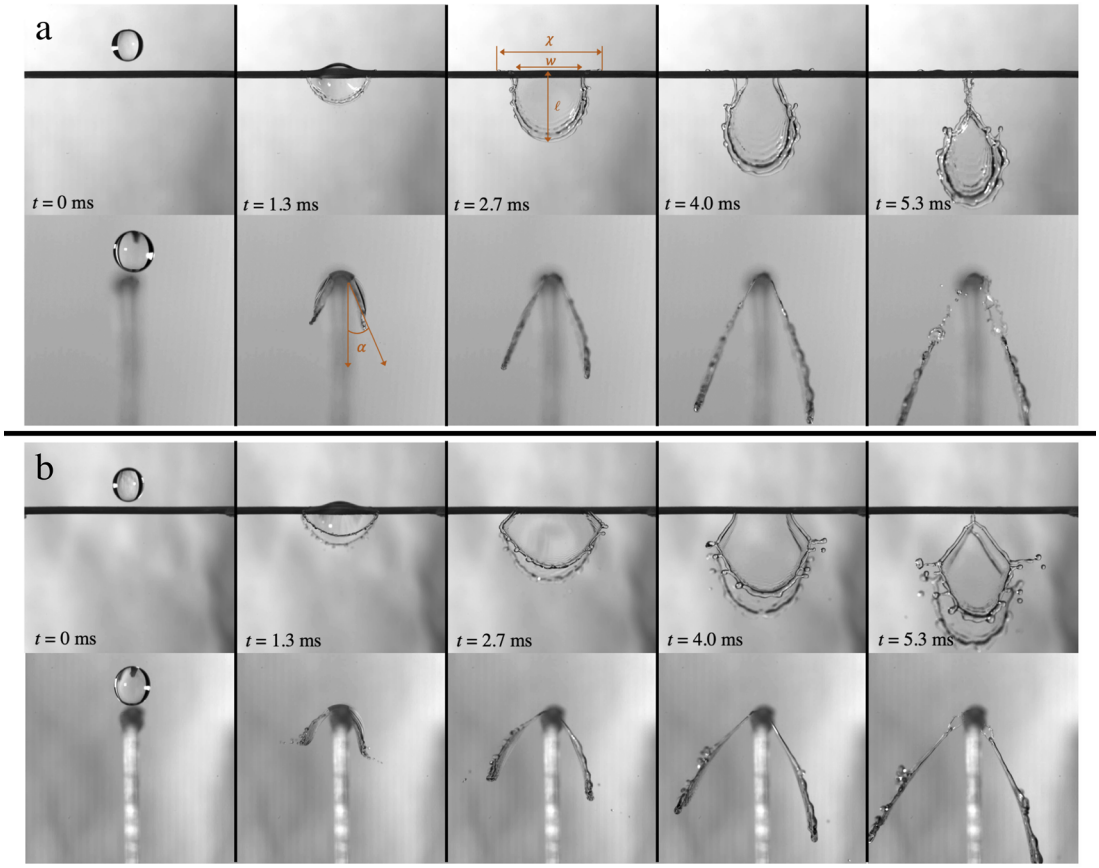

FIG. 1. Impact sequences. (a) A 3.9-mm diameter drop impacting a fixed pine needle with round profile facing the drop at U = 341 cm/s. We = 617. The top and bottom rows show simultaneous views, 90° opposed. (b) A 3.9-mm diameter drop impacting a fixed pine needle with wedge profile facing the drop at U = 347 cm/s. We = 656. The top and bottom rows show simultaneous views, 90° opposed.

drop breakup, spreading, and mass capture. Representative impact sequences for each fiber orientation are shown in Fig. 1. Drops impact our fibers over a Weber number range We = $\rho U^2 D/\sigma$ = 13–1270, where ρ = 1 g/cm^3 is the density of water, σ = 72.9 dyn/cm is the surface tension, U is the impact velocity, and D is the drop diameter. The Reynolds number range for our experiments Re = $\rho UD/\mu$ = 1670–2 × 10^4, where μ = 0.89 cP is the dynamic viscosity of water. Our horizontal, fixed fibers are green *Pinus*

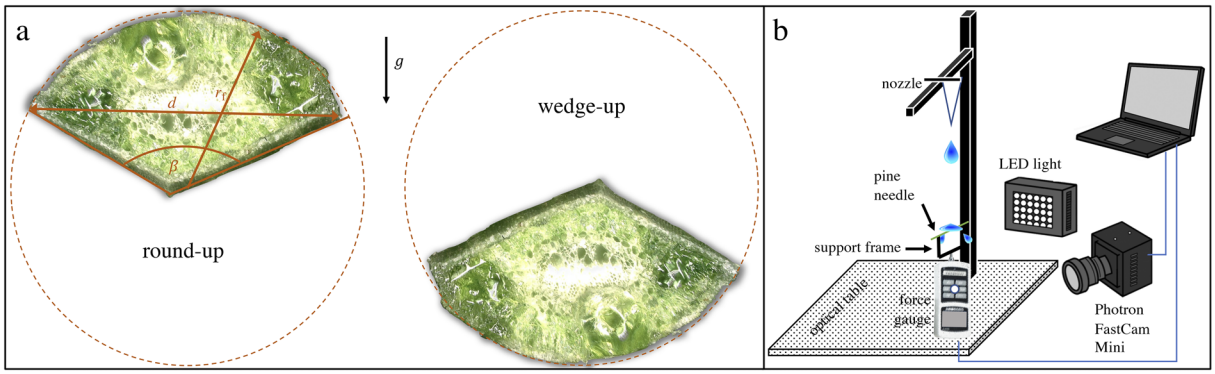

FIG. 2. (a) Cross section of a green *Pinus palustris* needle positioned in both experimental orientations. The round side has a circular radius of curvature r_f = 0.90 ± 0.04 mm and wedge angle β = 122.3° ± 8.3° (N = 4). (b) Experimental setup with the second camera not shown.

palustris needles, whose transverse cross sections are uniform. A typical cross section is shown in Fig. 2(a). All pines start with a single round proto-needle in the fascicle bud and split to form a number of final needles as they mature.[27] Species with two needles are approximately semi-circular in cross section, while those with three or more are wedge-shaped, comparable to cutting a pie into thirds, fourths, or fifths.[28,29] *In vivo* cross section orientation may be either of the two orientations we study here and anything in between. A cross section of three *Pinus palustris* needles in their fascicle sheath is shown in Fig. S1 of the supplementary material. While pine needles are convenient for incorporating non-circular fibers into impact studies, their use also informs the relationship between needle form and the environmental pressures of aggressive rainfall. Pine needles, like all foliage, reduce the kinetic energy of raindrops, which erode the soil underneath,[30–34] withstand high-speed raindrop impacts, and effectively shed water. Superfluous deflection promotes xylem vessel cavitation, damaging needle function.[35–37] We present our experimental methods in Sec. II and discuss results, theoretical considerations, and the implications of our work in Sec. III.

II. METHODS

Green pine needles are harvested from pine trees at the University of Central Florida's arboretum while still on the tree. Needles are sectioned and used for filming within 12 h and replaced every filming day, a protocol consistent with standard ecophysiology practice.[38] An entire dataset consisting of 12 drop velocities U, with 3 replicates, is performed with a single needle.

Our drop apparatus, schematized in Fig. 2(b), is constructed with a 165-cm tall 80/20 1530 extrusion tower affixed to a 91 × 183 cm optical table (Nexus, Thor Labs, Newton, NJ). Nozzles are positioned at 12 heights along the tower. Drops are produced by a syringe pump (New Era NE-1010). Two nozzles with inner diameters of 1.5 mm and 0.25 mm release larger, $D = 3.90 \pm 0.09$ mm (N = 66), and smaller, $D = 2.75 \pm 0.04$ mm (N = 72), drops. These drop sizes are within the range of natural rain[39] and simulate drops measured beneath a red pine canopy.[40] Pine needle fibers are rigidly secured to a 26-mm wide custom "goal post" with cyanoacrylate at both ends. This method of securing needles makes the influence of the needle stiffness negligible. The wooden goal post is adhered to the force gauge (MARK-10 Series 7 M7-012, Copiague, NY) with cyanoacrylate, which records force readings at 14 000 Hz. Impacts are illuminated by LED lights (GS Vitec MultiLED LT, Bad Soden–Salmünster, Germany) and filmed with two synchronized high speed cameras (Photron AX-200 and AX-100, Tokyo, Japan) at 3000 fps. The two cameras are set perpendicular to one another in the same plane to provide two orthogonal impact views (Fig. 1). Videos are analyzed with Open Source Physics Tracker and MATLAB (Mathworks, Natick, MA). The drop mass remaining on the fibers post-impact is collected by swabbing fibers with a small piece of absorbent fabric after each impact. The fabric is massed before and after swabbing using an analytical balance (Sartorius Secura 225D-1S, Göttingen, Germany) to quantify the captured drop mass.

The wetting properties of pine needles are measured using two methods. The single-fiber meniscus method is used to obtain the receding contact angle θ_r. A pine needle sample is withdrawn from a quiescent pool of water at a constant rate and a still image recorded using a digital microscope (Keyence VHX-900F, Osaka, Japan). The ImageJ software is used to find an average receding contact angle. The equilibrium contact angle θ_e and advancing contact angle θ_a are obtained from drop shape analysis of the sessile drop and captive needle methods, respectively. A camera is used to capture videos from which averages θ_e and θ_a are obtained.

III. RESULTS AND DISCUSSION

Fibers are impacted by drops at two orientations by rotating a freshly harvested *Pinus palustris* pine needle 180° such that either the rounded side [Fig. 1(a), Movies S1 and S2] or the wedged side [Fig. 1(b), Movies S3 and S4] of the cross section pierces the falling drop. We henceforth refer to these scenarios as "round-up" or "wedge-up" fibers. Drops are released from two nozzles such that they have diameters $D \approx 2.75$ mm and 3.90 mm as measured with a circle-fitter, subsequently referred to as "small" and "large" drops, respectively. Drops are released from 12 heights such that impact velocity $U = 54$ cm/s–484 cm/s, producing impacts lasting less than 10 ms. Pine needles have contact angles $\theta_a = 75° \pm 6°$ (N = 10), $\theta_e = 69° \pm 8°$ (N = 7), and $\theta_r = 32° \pm 5°$ (N = 22). Pine needle effective width $d = 1.56 \pm 0.05$ mm (N = 4) seen by the falling drop and radius of curvature $r_f = 0.90 \pm 0.04$ mm (N = 4), labeled in Fig. 2(a). We consider only centric impacts, where the fiber bisects the impacting drop. Eccentric impacts create dramatically non-symmetric lobes, as shown in Movie S5, and we posit slight eccentricities in our data contribute to variations in impact features. The role of eccentricity on impact properties is an area for future work.

If looking down the fiber axis, lobes flow away from the fiber at an angle of α [Fig. 1(a)], with respect to vertical, prior to lobe retraction and fragmentation. Impact velocities greater than those in this study would likely produce prompt splashing that fragments drops prior to lobe formation.[7,8,41] For round-up fibers, we observe a general range of $\alpha = 18°–26°$, as shown in Fig. 3(a), with weak monotonicity with We. Spearman's correlation coefficient $r_s = -0.29$ and $r_s = -0.23$ for large and small drops, respectively. For wedge-up, we observe a general range of $\alpha \approx 30°–50°$, with $r_s = 0.87$ and $r_s = -0.18$ for large and small drops, respectively. Experimental average values of separation angle $\bar{\alpha}$ are shown by the horizontal lines in Fig. 3(a). The observation for these shape-dependent ranges of α is rationalized by the wedge angle $\beta = 122° \pm 8°$ (N = 4), illustrated in Fig. 2(a). The angle β is determined by the number of needles in the sheath (Fig. S1), $\beta \approx 360°/3 = 120°$. The upper limit for α is set by completely tangential separation of the thin film from the round or wedged surfaces. For the round-up orientation, $\alpha < (180° - \beta)/2 \approx 29°$, and for wedge-up orientation $\alpha < \beta/2 \approx 61°$. Experimental values of α do not meet their tangential limits due to the influence of capillary forces at the separation point pulling the liquid film inward to the substrate.[2,42] This is particularly true for round-up fibers that are subject to the "teapot effect."

A. Drop spreading on the fiber

Drops spread down the fiber axis a maximum length χ within 3 ms after first contact, as labeled in Fig. 1(a). We observe for

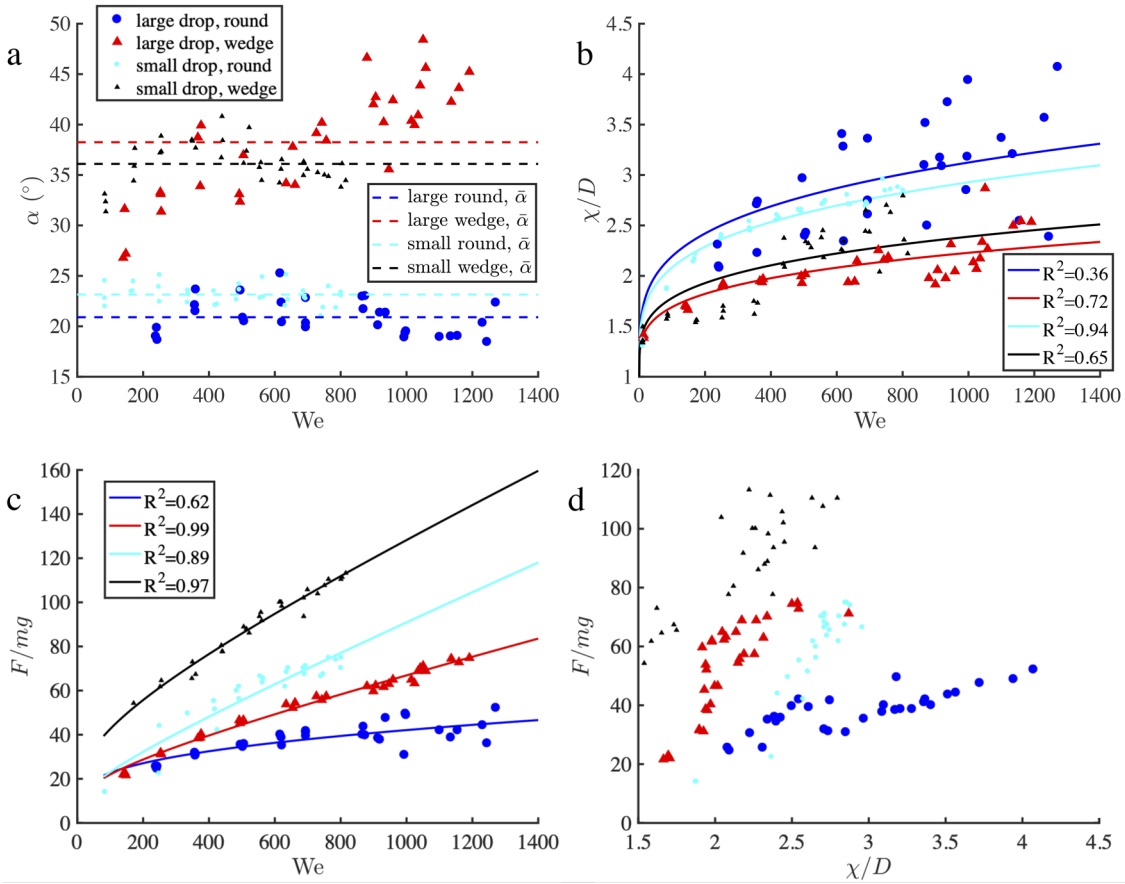

FIG. 3. Impact metrics. (a) Lobe separation angle vs Weber number. Dashed lines correspond to average separation angles, $\bar{\alpha}$, for respective impact conditions. The legend in the top-left corner of panel (a) applies to all panels. (b) Normalized maximum fiber wetted length vs Weber number. Correlation values correspond to Eq. (3). (c) Normalized impact force vs Weber number. Correlation values correspond to Eq. (6). (d) Normalized impact force vs normalized maximum fiber wetted length.

round-up fibers that at the moment of maximal spreading, the height of the descending parabolic lobes ℓ is approximately the width w of the lobe at the fiber [Figs. 1(a) and S2], $\ell/w = 0.95 \pm 0.05$ (N = 10) and $\ell/\chi = 0.64 \pm 0.09$ (N = 10). For wedge-up fibers $\ell/w = 0.64 \pm 0.04$ (N = 10) and $w \approx \chi$ [Figs. 1(b) and S2]. For simplicity, we take $\ell \sim w$ and $\ell \sim \chi$. The area of each parabolic lobe as viewed from the camera is thus $A \approx 2\ell^2/3$. The impact acceleration of the impinging drop onto the topmost surface of the fiber, $\lambda \sim U^2/D$, with a crashing time of $\Delta t \sim D/U$. As the drop strikes the fiber, the thickness of the newly formed lobe flowing from the fiber with angle α is set by[9,43,44]

$$l_c^* = \left(\frac{\sigma}{\rho\lambda}\right)^{\frac{1}{2}}. \tag{1}$$

The earliest stages of lobe projection have thicknesses <1 mm in our experiments, and one such example is pictured in Fig. S3 of the supplementary material. The leading edge of the lobe thickens to form the lobe rim as the leading edge decelerates.[44]

Volume conservation mandates that $\frac{\pi}{6}D^3 \approx 2l_c^* A$, and so combining the above relations, we may write

$$\chi/D \sim \mathrm{We}^{\frac{1}{4}}, \tag{2}$$

which matches the spreading relation for drops impacting a dry wall[9] when $\mathrm{WeRe}^{-4/5} < 1$, corresponding to an impact velocity of $U < 9.7$ m/s for our largest drops, a value exceeding the terminal velocity of raindrops.[1,45] There are no other relations for the spreading of a drop down a fiber in the literature, to the authors' knowledge.

Values of $\chi/D \approx 1.25$–4.5 in our experiments match those reported for spreading of a drop on a flat surface without rebound,[46,47] $\chi/D \approx 1.25$–5. We note that $\chi \neq 0$ as $\mathrm{We} \to 0$, a statement rationalized by observing that if $U \approx 0$ and the drop is captured by the fiber,[18,19,26] the drop will wet the fiber such that $\chi/D \approx 1$. Furthermore, as wedged fibers approach infinitesimally thin slivers, i.e., $\beta \to 0$, the drop will not spread on impact, $\chi/D = 1$. Thus, we submit a modification to Eq. (2) to correct for these limits,

$$\chi/D = C_1 \mathrm{We}^{\frac{1}{4}} + 1, \tag{3}$$

where C_1 is a fitting parameter.

Non-dimensionalized wetting length χ/D is plotted against We in Fig. 3(a), with curves generated by Eq. (3) and associated correlation values printed in the figure. Spreading qualitatively behaves according to the prediction of Eq. (3), and we find reasonable agreement with all curves but the large drop impacting the rounded face of the fiber, perhaps due to early impact fragmentation as discussed below. It is noteworthy that the drop spreads along the wedge-up axis to a greater extent at the wedge bottom than the sharp peak, as shown in the middle panel of Figs. 1(b) and S2. All our data are admittedly noisy, a possible consequence of small impact eccentricities, drop flattening on descent, and defects in the fiber surface. The experimental noise in the data does not permit large correlation values.

For comparison, we consider the relation by Scheller and Bousfield[48] for impacts on a flat, dry surface that do not recoil or rebound. They report $\chi/D = 0.61(\mathrm{We/Oh})^{0.166}$, where the Ohnesorge number $\mathrm{Oh} = \mu/(\rho\sigma D)^{1/2}$. While the behavior of the power law given by Scheller and Bousfield (1995) well describes the shape of χ/D curves (Fig. S4), the magnitude of the prefactor overestimates the spreading down the fiber, indicating drops spread more extensively on flat surfaces than fibers due to non-axisymmetric lobes. We fit

$$\chi/D = C_2(\mathrm{We/Oh})^{C_3} \tag{4}$$

to our data and report the values of fitting parameters C_2 and C_3 in Table I. Exponents are near that given in the work of Scheller and Bousfield[48] for small drops.

B. Impact force

Prior to the maximum extension of the lobes, a maximum impact force F is measured, occurring ~2 ms after the initial contact. An example of the force gauge's digital output is shown in Fig. S5 of the supplementary material. The needle's supporting apparatus and gauge [Fig. 2(b)] behave as a highly underdamped oscillator, and we thus take the maximum force value of the gauge output as the measure of impact force. Impact force increases at greater We, as shown in Fig. 3(c). Drops undergoing greater deformation and spreading a greater distance down the fiber are associated with higher impact forces. We plot F/mg vs χ/D in Fig. 3(d) and find that increased F is associated with increased χ, and for a fixed value of χ/D, wedge-up fibers experience greater values of F/mg. Dimensional F vs We is shown in Fig. S6, which clearly reveals wedge-up fibers receive greater impact forces for a fixed drop size.

The impulse of drop impact decreases the drop momentum, and a force balance takes the following form:

$$m\left(U - U'\right) = (F_\mathrm{d} + F_\mathrm{s} + mg)\Delta t, \tag{5}$$

where U' is the velocity of the fluid mass post-collision, to include the velocity of any mass captured by the fiber, m is the drop mass, and $\Delta t \sim D/U$ is the contact time with the fiber. Since $d/D < 1$ in our system,[17] the pressure imposed by the passing drop on the top surface of the fiber is $\sim(1/2)\rho U^2$. Fluid leaving the fiber at an angle α, at early stages of impact when viscous effects are not yet significant and force is greatest, modulates the drag force such that[43] $F_\mathrm{d} \sim (1/2)\rho U^2 Dd(1 - \cos\alpha) \sim \frac{1}{2}d\sigma\mathrm{We}(1 - \cos\alpha)$. Such a formulation for F_d assumes the film impacting and leaving the fiber does not change thickness.[17] Deformation of the drop surface increases the surface energy, scaling with the lobe size, $\sim\sigma A$. We thus expect the related surface force deformation $F_\mathrm{s} \sim \sigma\chi$. Combining Eqs. (2) and (5), we may write

$$F/mg \sim (\sigma g/\rho)\left[dD^{-3}(1 - \cos\alpha)\mathrm{We} + D^{-2}\mathrm{We}^{\frac{1}{4}}\right] + 1, \tag{6}$$

which permits $F \sim mg$ when $U = 0$.

We plot F/mg vs We in Fig. 3(c) and provide correlation values for $F/mg = C_4\mathrm{We} + C_5\mathrm{We}^{1/4} + 1$ in the figure, where C_4 and C_5 are fitting parameters. Wedged fibers create greater splitting of impact lobes, coinciding with greater $\tilde{\alpha}$. The larger 3.90-mm drop imparts greater force than the smaller 2.75-mm drop for both fiber profiles, and F grows with increasing We. We note the curves in Fig. 3(b) do not collapse on one another, and thus, definition of a correction factor to Eq. (6) that is a function of drop size and fiber orientation is an area for future work. Proper definition of such a factor will require systematic variance of drop diameter and wedge angle while sweeping through a range of drop velocity.

The variance in force for We > 800 when the large drop impacts the rounded side of the needle results in a low correlation value $R^2 = 0.57$. The source of this variance is unknown but is perhaps a result of the "prompt splash," or detached droplets at the leading edge of the lobe periphery for the fastest impacts.[7,8,41] An example of leading edge fragmentation for We = 1000 can be seen in Fig. S7 of the supplementary material. For the wedge-up condition, best fits are in very good agreement with the predicted fit in Eq. (6).

TABLE I. Correlation values and best fit exponents for the spreading relation posed by Scheller and Bousfield.[48]

Drop size	Orientation	$\chi/D = d(\mathrm{We/Oh})^f$
Large	Round	$C_2 = 0.08$, $C_3 = 0.24$, $R^2 = 0.40$
	Wedge	$C_2 = 0.36$, $C_3 = 0.12$, $R^2 = 0.70$
Small	Round	$C_2 = 0.22$, $C_3 = 0.18$, $R^2 = 0.99$
	Wedge	$C_2 = 0.16$, $C_3 = 0.19$, $R^2 = 0.70$

C. Lobe evolution

Lobes formed by impacting drops resemble the lamellae formed by drops striking bells,[44] spheres,[2,50] discs,[43] and cups.[51] Lobes reach a maximum spread on the fiber χ within 3 ms, and as lobes continue to fall, the liquid film on the fiber retracts as shown by the temporal traces in Fig. 4. Generally, the lobes formed by round-up fibers have fewer fingers and a more clearly defined rim than those of wedge-up fibers. Capillary forces ultimately pinch off lobes near the fiber (Fig. 1) at which point the now free lobe rapidly contracts toward its center of mass, as shown in the supplementary material.

The temporal position of the bottom of the falling drop is plotted for time <0 in Figs. 5(a) and 5(b), whereas the position of lobe

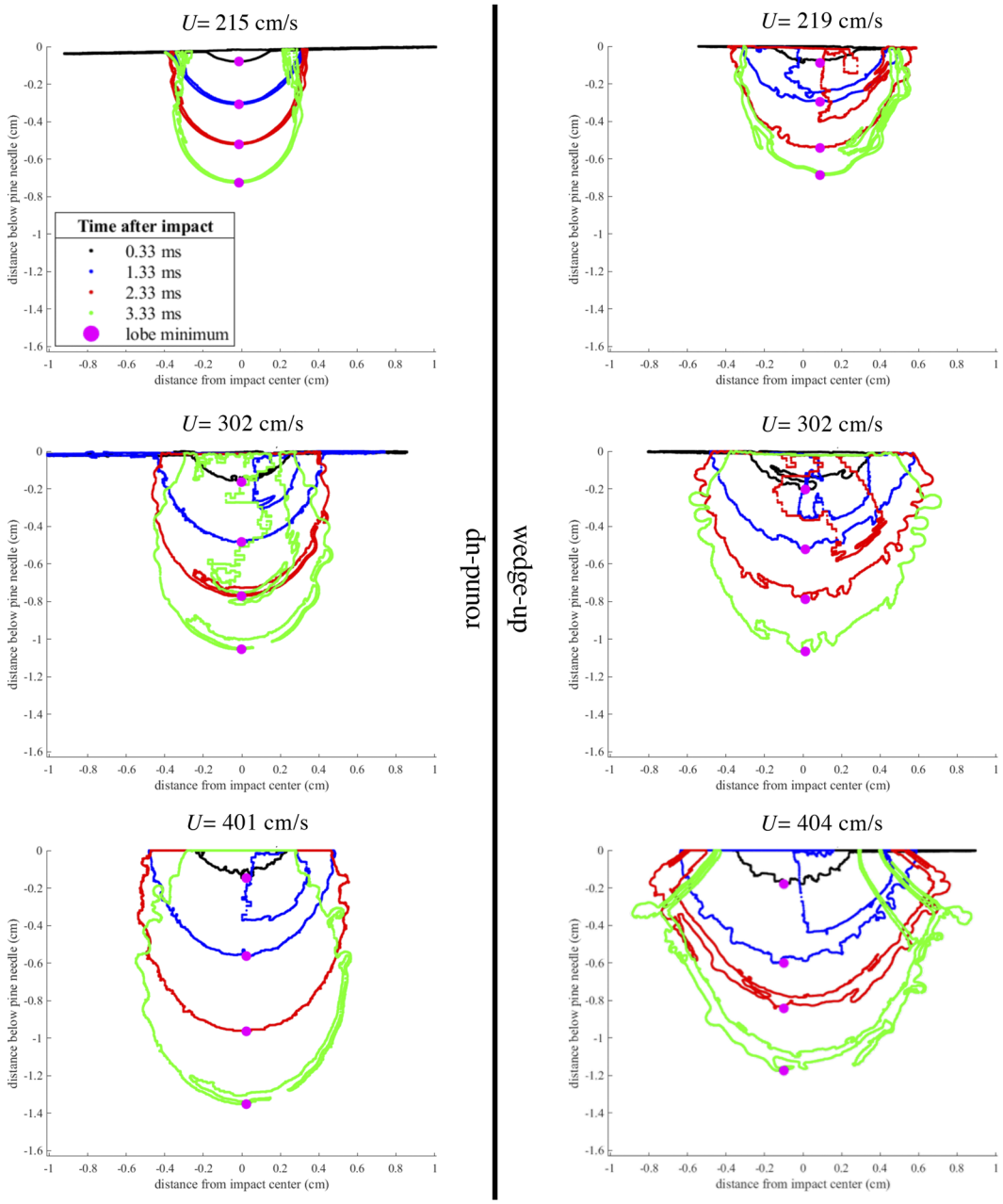

FIG. 4. Traces of lobe edges at four discrete times from impact, done by code adapted from that developed by de Ruiter *et al.*[49] Due to capillary wave expression inside the lobes, some pixels within lobes have intensity values that are difficult to differentiate from pixels on lobe edges. This results in the code occasionally misidentifying boundaries, but does not affect lobe tracking. The true lobes are the outermost traces in each color.

minima (bottom-most point on lobe rim) is plotted for time >0. We provide four impact speeds onto both fiber orientations for large [Fig. 5(a)] and small [Fig. 5(b)] drops. Normalized lobe minima velocity U_{lobe}/U is plotted in Figs. 5(c) and 5(d) for large and small drops, respectively. Position data are smoothed with a moving average filter to reduce experimental noise before and after numerical differentiation. Lobe minima slow their velocity as lobes expand. The decrease in lobe minima velocity with time indicates capillarity, viscosity, and aerodynamic drag balance what would otherwise be the gravitational increase in velocity as lobes fall.

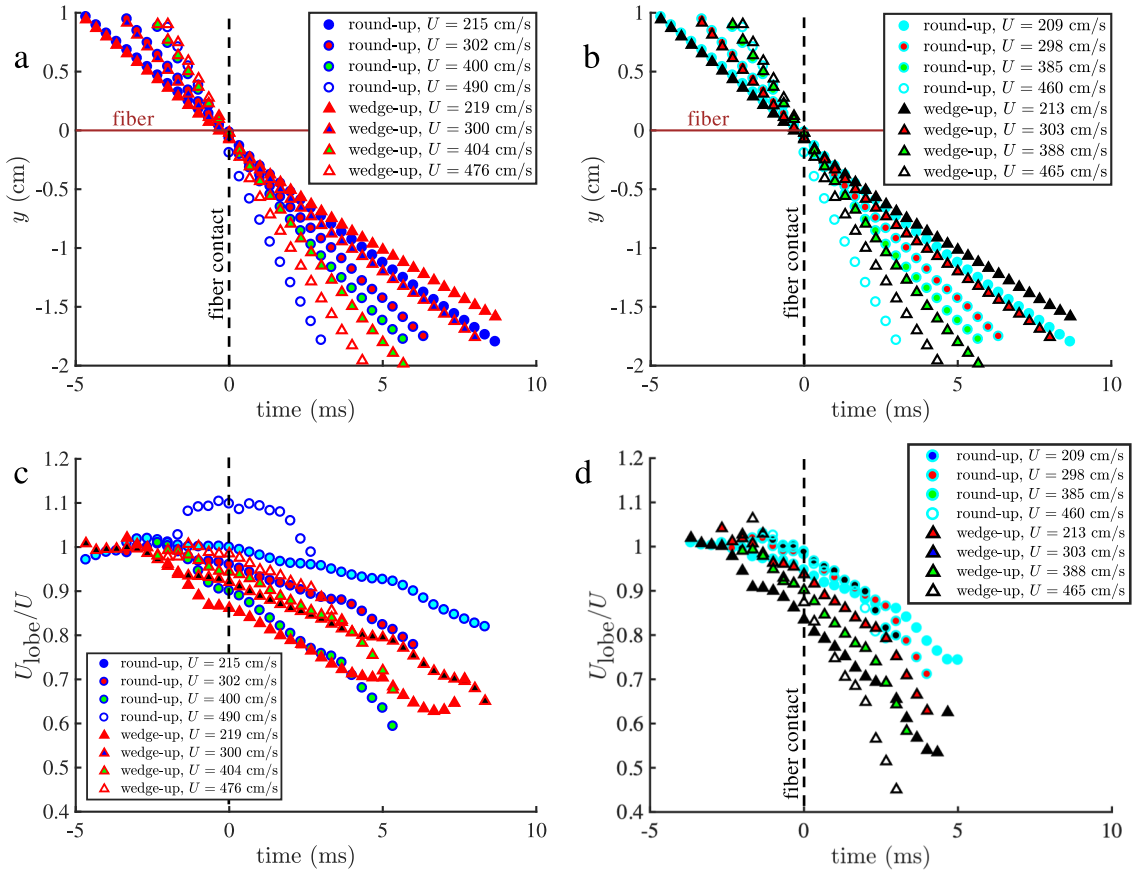

FIG. 5. Lobe tracking. (a) Drop/lobe minima position tracks of large drops impacting fibers at various speeds. (b) Drop/lobe minima position tracks of small drops impacting fibers at various speeds. (c) Normalized lobe velocity for the tracks shown in (a). (d) Normalized lobe velocity for the tracks shown in (b). Data are smoothed with a moving average filter for the entire data span.

For a fixed drop velocity, lobes emanating from round-up fibers fall ≈10% faster than from wedge-up fibers with few exceptions. The kinetic energy of a falling drop drives lobe projection, and thus, thinner lobes travel faster. A detailed analysis of drop deformation that governs the lobe thickness is non-trivial because the flow is relatively complicated and governed by viscous, inertial, and capillary forces.[46,50,52] Drops impacting a rounded fiber encounter a surface that has a horizontal tangent, producing greater horizontal flow and thinner lobes in the earliest stage of impact. For a sharp wedge, the surface tangent lies at an angle $(180^\circ - \beta)/2$ with respect to the horizontal. We thus posit the resulting impact acceleration is reduced by $\sin(\beta/2)$. In the limit of wedges with very small β, we do not expect drops to form lobes.

D. Mass retention

Following impact, a portion of the drop remains on the fiber, m_c. The ratio of $m_c/m \approx 0$–0.49 is shown in Fig. 6(a). At no impact speed is the entire drop captured; capture requires either a lower contact angle, higher viscosity, or slower drop speed. However, at the lowest We ≈ 11, fibers retain much greater mass than the bulk of experiments, suggesting our slowest trials are approaching drop capture, as shown in the inset of Fig. 6(a). It was previously found m_c/m remains unchanged with the drop volume, which is supported by our results for wedge-up fibers. Excluding large drop on round-up data, due to copious experimental noise, we rationalize our experimental observations with scaling analysis. We assume drop retention will scale with the product of wetted fiber area and lobe thickness, $m_c \sim \rho A_w \ell_c^*$. Round-up fibers have a wetting area $A_w \approx \beta r_f \chi$, where βr_f is the arc length of the rounded side. Wedge-up fibers have a wetted area $A_w \approx 2 r_f \chi$. Using Eqs. (1) and (2), we may write for round-up fibers,

$$m_c/m \sim \beta r_f \mathrm{We}^{-1/4} D^{-1}, \tag{7}$$

omitting all constants. For wedge-up fibers,

$$m_c/m \sim r_f \mathrm{We}^{-1/4} D^{-1}, \tag{8}$$

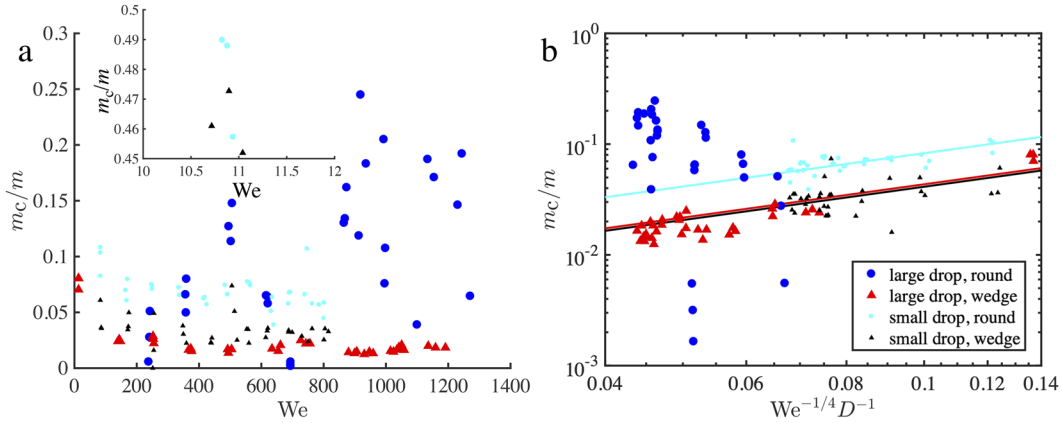

FIG. 6. Retained drop mass. (a) Dependence of non-dimensionalized captured drop mass on We. (b) Dependence of non-dimensionalized captured drop mass on $\mathrm{We}^{-1/4}D^{-1}$. The inset in (a) extends the plotted range, and the legend in (b) applies to both panels.

omitting all constants. Noting that β and r_f are constant in our experiments, we plot the dependence of m_c/m vs $\mathrm{We}^{-1/4}D^{-1}$ in Fig. 6(b), and note our data follow the trends of Eqs. (7) and (8) with the exception of large drops impacting the round-up fiber (dark blue points). Scatter in the data does not permit high correlation values, however. Data for the smallest We values [inset of Fig. 6(a)] have been omitted in Fig. 6(b) because the drop deforms without forming lobes, and thus, our scaling relations in Eqs. (7) and (8) do not apply. The dependence of m_c on χ is plotted in Fig. S8.

Kim and Kim[17] suggested that mass retention by a rigid, horizontal, circular fiber may be scaled as $m_c/m \sim (d/D)^2\mathrm{Re}^{-1/2}$ and saw greater levels of retention on their fibers of comparable wetting properties to ours. We plot the line of best fit to the Kim and Kim[17] data against our data in Fig. S9. Excluding round-up data for large drops, m_c/m values for our fibers are on average 2.3×–4.8× lower than the values reported by Kim and Kim (2016). The non-circular profile of our needles is more effective at water shedding when compared to circular fibers. Thus, we show that cross sections of non-circular fibers may be tuned against mass retention. Our results are perhaps unsurprising when considering the evolutionary pressures that have shaped the form of pine needles; water retention on needles is not an advantage. Leaves that do not shed water effectively retain a film of water on the leaf cuticle for long periods of time, blocking the exchange of carbon dioxide and water vapor through leaf stomata,[53] leaching valuable nutrients from foliage,[54,55] and promoting disease.[53] Water films inhibit photosynthesis, and if a chronic occurrence, can reduce the plant productivity and growth rate.[56,57] The cross section of our needles thus appears tuned to reduce water retention following raindrop strikes, particularly as the relatively fast speed of raindrops[45] pushes We past what we are able to produce.

As We grows, the force of impact rises as the retained mass tends to decrease. This apparent trade-off implies that the evolutionary pressure of water shedding is more dominant than the need to reduce impact forces. An area for future work will be the study of forces and water shedding for needles in a natural setting in which they are cantilevered and obliquely oriented toward incoming drops. We surmise that oblique impacts will favor retention while reducing force and that longer needles are more prone to retention. Cross sections will vary with the number of needles per fascicle, and those with smaller β values, which can be as low as 72°, will be more effective at splitting drops, retaining less mass and perhaps experiencing smaller forces. Smaller and more hydrophobic needles are likely to retain less mass than our specimens,[15] though how wetting properties influence the impact force is understudied. The water shedding properties of non-circular fibers enjoyed by hundreds of species of conifers may likely be found in other plants with needle-like leaves of cross-sectional dimension comparable to raindrops, such as rosemary (*Lamiaceae*), dill (*Anethum graveolens*), and purple needlegrass (*Nassella pulchra*).

IV. CONCLUSION

We have studied the impact of falling water drops with horizontal, fixed pine needles for two dissimilar orientations of their non-circular cross section. The wedge-up orientation produces a greater angle of separation of the liquid lobes formed by the impacting drop, compared to round-up fibers, and a corresponding larger impact force. The impact force and spreading of the drops down the fibers increase with the Weber number, and the scaling of such is well characterized by stagnation pressure and surface deformation scaling. Lobes extend downward at a speed nearly equal to the drop speed at impact and are more greatly fingered for wedge-up fibers. Fibers oriented wedge-up were less prone to mass capture than round-up fibers. Across the range of Weber number tested, pine needle fibers generally exhibited less mass retention post-impact than fibers with circular cross sections. Pine needles thus appear tuned to reject the accumulation of moisture by falling rain.

SUPPLEMENTARY MATERIAL

See the supplementary material for six movies and a supplementary document. The document contains descriptions of movies,

a fascicle bud image, a force gauge output plot, three additional impact images, and plots for χ/D vs We/Oh, F vs We, m_c vs χ, and m_c/m vs $(d/D)^2\mathrm{Re}^{-1/2}$.

ACKNOWLEDGMENTS

The authors would like to thank the University of Central Florida and NSF (Grant No. CBET-1941341) for financial support, Karim Kodieh and Jacob Biery for experimental assistance, and Dr. Rachel Pepper for providing lobe tracing MATLAB scripts.

DATA AVAILABILITY

Raw experimental videos and data are available in perpetuity via Open Science Framework: https://osf.io/tmu34/.

REFERENCES

[1]A. K. Dickerson, P. G. Shankles, N. M. Madhavan, and D. L. Hu, "Mosquitoes survive raindrop collisions by virtue of their low mass," Proc. Natl. Acad. Sci. U. S. A. **109**, 9822–9827 (2012).
[2]A. K. Dickerson, P. G. Shankles, and D. L. Hu, "Raindrops push and splash flying insects," Phys. Fluids **26**, 027104 (2014).
[3]A. K. Dickerson, X. Liu, T. Zhu, and D. L. Hu, "Fog spontaneously folds mosquito wings," Phys. Fluids **27**, 021901 (2015).
[4]M. E. Alam, J. L. Kauffman, and A. K. Dickerson, "Drop ejection from vibrating damped, dampened wings," Soft Matter **16**, 1931–1940 (2020).
[5]J. Ju, H. Bai, Y. Zheng, T. Zhao, R. Fang, and L. Jiang, "A multi-structural and multi-functional integrated fog collection system in cactus," Nat. Commun. **3**, 1247 (2012).
[6]T. Frising, D. Thomas, D. Bémer, and P. Contal, "Clogging of fibrous filters by liquid aerosol particles: Experimental and phenomenological modelling study," Chem. Eng. Sci. **60**, 2751–2762 (2005).
[7]E. Villermaux and B. Bossa, "Drop fragmentation on impact," J. Fluid Mech. **668**, 412–435 (2011).
[8]A. L. Yarin, "Drop impact dynamics: Splashing, spreading, receding, bouncing. . .," Annu. Rev. Fluid Mech. **38**, 159–192 (2006).
[9]C. Clanet, C. Béguin, D. Richard, and D. Quéré, "Maximal deformation of an impacting drop," J. Fluid Mech. **517**, 199–208 (2004).
[10]W. Gu, S. Yan, and Z. Bai, "A study on a droplet impact on a fiber during coalescence-separation: Phenomena and models," Chem. Eng. Sci. **212**, 115337 (2020).
[11]P. Zhu, W. Wang, X. Chen, F. Lin, X. Wei, C. Ji, and J. Zou, "Experimental study of drop impact on a thin fiber," Phys. Fluids **31**, 107102 (2019).
[12]H. Zhang, X. Yi, Y. Du, R. Zhang, X. Zhang, F. He, F. Niu, and P. Hao, "Dynamic behavior of water drops impacting on cylindrical superhydrophobic surfaces," Phys. Fluids **31**, 032104 (2019).
[13]M.-J. Su, Y. Luo, G.-W. Chu, Y. Cai, Y. Le, L.-L. Zhang, and J.-F. Chen, "Dispersion behaviors of droplet impacting on wire mesh and process intensification by surface micro/nano-structure," Chem. Eng. Sci. **219**, 115593 (2020).
[14]Y.-Y. Tang, M.-J. Su, G.-W. Chu, Y. Luo, Y.-Y. Wang, L.-L. Zhang, and J.-F. Chen, "Impact phenomena of liquid droplet passing through stainless steel wire mesh units," Chem. Eng. Sci. **198**, 144–154 (2019).
[15]H. Aziz, N. M. Farhan, and H. V. Tafreshi, "Effects of fiber wettability and size on droplet detachment residue," Exp. Fluids **59**, 122 (2018).
[16]M. Safavi and S. Nourazar, "Experimental, analytical, and numerical study of droplet impact on a horizontal fiber," Int. J. Multiphase Flow **113**, 316–324 (2018).
[17]S.-G. Kim and W. Kim, "Drop impact on a fiber," Phys. Fluids **28**, 042001 (2016).
[18]J. Comtet, B. Keshavarz, and J. W. M. Bush, "Drop impact and capture on a thin flexible fiber," Soft Matter **12**, 149–156 (2016).
[19]E. Dressaire, A. Sauret, F. Boulogne, and H. A. Stone, "Drop impact on a flexible fiber," Soft Matter **12**, 200–208 (2016).
[20]Y. Wang, "Numerical study of a droplet impact on cylindrical objects: Towards the anti-icing property of power transmission lines," Appl. Surf. Sci. **516**, 146155 (2020).
[21]S. Wang and O. Desjardins, "Numerical study of the critical drop size on a thin horizontal fiber: Effect of fiber shape and contact angle," Chem. Eng. Sci. **187**, 127–133 (2018).
[22]X. Dong, X. Huang, and J. Liu, "Modeling and simulation of droplet impact on elastic beams based on SPH," Eur. J. Mech., A: Solids **75**, 237–257 (2019).
[23]J. Zheng, J. Wang, Y. Yu, and T. Chen, "Hydrodynamics of droplet impingement on a thin horizontal wire," Math. Probl. Eng. **2018**, 9818494.
[24]S. Abishek, R. Mead-Hunter, A. King, and B. Mullins, "Capture and re-entrainment of microdroplets on fibers," Phys. Rev. E **100**, 042803 (2019).
[25]N. Ojaghlou, H. V. Tafreshi, D. Bratko, and A. Luzar, "Dynamical insights into the mechanism of a droplet detachment from a fiber," Soft matter **14**, 8924–8934 (2018).
[26]K. Piroird, C. Clanet, É. Lorenceau, and D. Quéré, "Drops impacting inclined fibers," J. Colloid Interface Sci. **334**, 70–74 (2009).
[27]D. Richardson, *Ecology and Biogepgraphy of Pinus* (Cambridge University Press, 2000).
[28]D. Wyman, "Simple key to the pines," Arnoldia **11**(9), 63–70 (1943); available at http://arnoldia.arboretum.harvard.edu/pdf/articles/1951-11–simple-key-to-the-pines.pdf
[29]V. M. Dörken and T. Stützel, "Morphology, anatomy and vasculature of leaves in *Pinus* (Pinaceae) and its evolutionary meaning," Flora—Morphol., Distrib., Funct. Ecol. Plants **207**, 57–62 (2012).
[30]S. R. Herwitz, "Raindrop impact and water flow on the vegetative surfaces of trees and the effects on stem flow and through fall generation," Earth Surf. Processes Landforms **12**, 425–432 (1987).
[31]M. A. Nearing, F. F. Pruski, and M. O'neal, "Expected climate change impacts on soil erosion rates: A review," J. Soil Water Conserv. **59**, 43–50 (2004).
[32]G. B. Williamson, A. Romero, J. K. Armstrong, T. J. Gush, A. J. Hruska, P. E. Klass, and J. T. Thompson, "Driptips, drop size and leaf drying," Biotropica **15**, 232–234 (1983).
[33]G. B. Williamson, *Driptips and Splash Erosion* (Biotropica, 1981), pp. 228–231.
[34]M. Beczek, M. Ryzak, A. Sochan, R. Mazur, C. Polakowski, and A. Bieganowski, "The differences in crown formation during the splash on the thin water layers formed on the saturated soil surface and model surface," PLoS One **12**, e0181974 (2017).
[35]H. A. Cleugh, J. M. Miller, and M. Böhm, "Direct mechanical effects of wind on crops," Agroforestry Syst. **41**, 85–112 (1998).
[36]J. Grace, "Plant response to wind," in *Windbreak Technology* (Elsevier, 1988), pp. 71–88.
[37]S. Hoad, C. Jeffree, and J. Grace, "Effects of wind and simulated acid mist on leaf cuticles," in *Air Pollutants and the Leaf Cuticle* (Springer, 1994), pp. 225–237.
[38]N. Pérez-Harguindeguy, S. Díaz, E. Garnier, S. Lavorel, H. Poorter, P. Jaureguiberry, M. S. Bret-Harte, W. K. Cornwell, J. M. Craine, D. E. Gurvich *et al.*, "New handbook for standardised measurement of plant functional traits worldwide," Aust. J. Bot. **61**, 167–234 (2013).
[39]A. Nouhou Bako, F. Darboux, F. James, C. Josserand, and C. Lucas, "Pressure and shear stress caused by raindrop impact at the soil surface: Scaling laws depending on the water depth," Earth Surf. Processes Landforms **41**, 1199–1210 (2016).
[40]G. Chapman, "Size of raindrops and their striking force at the soil surface in a red pine plantation," EOS, Trans. Am. Geophys. Union **29**, 664–670 (1948).
[41]R. Rioboo, C. Tropea, and M. Marengo, "Outcomes from a drop impact on solid surfaces," Atomization Sprays **11**, 155–165 (2001).
[42]C. Duez, C. Ybert, C. Clanet, and L. Bocquet, "Wetting controls separation of inertial flows from solid surfaces," Phys. Rev. Lett. **104**, 084503 (2010).
[43]A. Rozhkov, B. Prunet–Foch, and M. Vignes–Adler, "Dynamics of a liquid lamella resulting from the impact of a water drop on a small target," Proc. R. Soc. London, Ser. A **460**, 2681 (2004).
[44]A. Rozhkov, B. Prunet-Foch, and M. Vignes-Adler, "Impact of water drops on small targets," Phys. Fluids **14**, 3485 (2002).

[45]R. Gunn and G. D. Kinzer, "The terminal velocity of fall for water droplets in stagnant air," J. Meteorol. **6**, 243–248 (1949).
[46]R. Rioboo, M. Marengo, and C. Tropea, "Time evolution of liquid drop impact onto solid, dry surfaces," Exp. Fluids **33**, 112–124 (2002).
[47]Š. Šikalo, M. Marengo, C. Tropea, and E. Ganić, "Analysis of impact of droplets on horizontal surfaces," Exp. Therm. Fluid Sci. **25**, 503–510 (2002).
[48]B. L. Scheller and D. W. Bousfield, "Newtonian drop impact with a solid surface," AIChE J. **41**, 1357–1367 (1995).
[49]J. de Ruiter, R. E. Pepper, and H. A. Stone, "Thickness of the rim of an expanding lamella near the splash threshold," Phys. Fluids **22**, 022104 (2010).
[50]S. Bakshi, I. V. Roisman, and C. Tropea, "Investigations on the impact of a drop onto a small spherical target," Phys. Fluids **19**, 032102 (2007).
[51]G. J. Amador, Y. Yamada, M. McCurley, and D. L. Hu, "Splash-cup plants accelerate raindrops to disperse seeds," J. R. Soc., Interface **10**(79), 20120880 (2013).
[52]I. V. Roisman, R. Rioboo, and C. Tropea, "Normal impact of a liquid drop on a dry surface: Model for spreading and receding," Proc. R. Soc. London, Ser. A **458**, 1411 (2002).
[53]T. E. Dawson and G. R. Goldsmith, "The value of wet leaves," New Phytol. **219**, 1156–1169 (2018).
[54]T.-C. Lin, S. P. Hamburg, Y.-J. Hsia, H.-B. King, L.-J. Wang, and K.-C. Lin, "Base cation leaching from the canopy of a subtropical rainforest in northeastern Taiwan," Can. J. For. Res. **31**, 1156–1163 (2001).
[55]C. E. Oyarzún, R. Godoy, A. De Schrijver, J. Staelens, and N. Lust, "Water chemistry and nutrient budgets in an undisturbed evergreen rainforest of southern Chile," Biogeochemistry **71**, 107–123 (2004).
[56]M. A. Jenks and E. N. Ashworth, "Plant epicuticular waxes: Function, production, and genetics," Hortic. Rev. **23**, 1–68 (1999).
[57]W. K. Smith and T. M. McClean, "Adaptive relationship between leaf water repellency, stomatal distribution, and gas exchange," Am. J. Bot. **76**, 465–469 (1989).